UNIVERSIDADE ESTADUAL DE CAMPINAS
SISTEMA DE BIBLIOTECAS DA UNICAMP
REPOSITÓRIO DA PRODUÇÃO CIENTIFICA E INTELECTUAL DA UNICAMP

Versão do arquivo anexado / Version of attached file:

Versão do Editor / Published Version

Mais informações no site da editora / Further information on publisher's website:

https://www.ingentaconnect.com/contentone/asp/jnn/2018/00000018/00000005/art00044

DOI: 10.1166/jnn.2018.14659

Direitos autorais / Publisher's copyright statement:

Pt-CeO$_2$ Catalysts Synthesized by Glucose Assisted Hydrothermal Method: Impact of Calcination Parameters on the Structural Properties and Catalytic Performance in PROX-CO

Diego R. Carvalho, Isaias B. Aragao, and Daniela Zanchet*

Institute of Chemistry, University of Campinas–UNICAMP, C.P. 6154, 13083-970, Campinas, SP, Brazil

We synthesized Pt supported catalysts by the glucose assisted hydrothermal method, in which a carbon template was used to form a porous CeO$_2$ structure upon calcination. Special emphasis was given to evaluate the influence of calcination parameters in the structural and textural properties of the catalysts and the final impact in the catalytic activity of CO oxidation reaction under hydrogen rich atmosphere (PROX-CO). We show that at 350 °C the carbon matrix was already mostly burnt and that higher temperatures and holding times mostly increase the CeO$_2$ crystallite sizes. The sample prepared at 350 °C presented the highest surface area, 106 m$^2 \cdot$g^{-1}, in comparison to 60–70 m$^2 \cdot$g^{-1} obtained for all other conditions. Transmission electron microscopy images of the catalyst calcined at 600 °C for 6 h showed 200 nm spheres formed by aggregation of ceria crystallites with crystalline domains of about 20 nm. All samples showed similar catalytic activity in PROX-CO indicating that the creation of the catalytic sites were mostly determined during the synthesis conditions and the catalytic performance were not deeply affected by the differences on CeO$_x$ matrix.

Keywords: Platinum Catalysts, CeO$_2$, Calcination, PROX-CO.

1. INTRODUCTION

Alternatives for energy production to provide both high energy efficiency and low waste generation are currently on demand. Among them, the polymer electrolyte membrane fuel cell (PEMFC) has attracted visibility due to its low operation temperature for portable and/or mobile applications.[1-4] The energy vector used in PEMFC is hydrogen (H$_2$), usually obtained from catalytic reforming of hydrocarbons, alcohol and biomass.[5-7] This H$_2$ stream carries large amounts of carbon monoxide (CO), which is a poison for PEMFCs, requering a purification sector. One of the most appealing alternatives to decrease the CO to acceptable levels (typically < 10 ppm) involves its conversion to CO$_2$ by preferential CO oxidation reaction on hydrogen rich stream (PROX-CO). The typical inlet stream of PROX-CO system is a rich mixture of H$_2$ (>70%) with appreciable amounts of H$_2$O (10–15%) and CO$_2$ (10–15%), besides CO (~1%). As a consequence,

besides CO oxidation, reactions such as H$_2$ oxidation, water gas shift, and methanation may compete.[8] A good catalyst for PROX-CO has to exhibit high CO conversion and high selectivity toward CO$_2$. Therefore, it is necessary to develop suitable catalysts for these reaction conditions.

Catalysts composed of noble metals, mostly gold and platinum, supported in metal oxides have been largely studied in the literature;[9-14] rhodium, ruthenium, silver and iridium supported catalysts have also been evaluated.[15, 16] The temperature range for the PROX-CO reaction in noble metal-based catalysts is typically between 80 and 200 °C and platinum-based catalysts have received special attention due to their excellent performance, with high activity and selectivity in this range of temperature. Marino et al.[16] evaluated platinum, palladium and iridium catalysts in PROX-CO reactions; while platinum and iridium catalysts showed similar performance, they were better than the palladium catalyst. Huang et al.[17] observed that platinum leads to lower methane production than ruthenium.

---

*Author to whom correspondence should be addressed.

The supports for PROX-CO reaction may also have an important role and can be grouped in two main groups: reducible and non-reducible supports. Marino et al.[18] studied the influence of several supports, such as CeO$_2$, SiO$_2$–Al$_2$O$_3$, Al$_2$O$_3$, SiO$_2$, La$_2$O$_3$ and MgO, in platinum-based catalysts; these supports have different acidic, basic and redox properties and the results showed that although acidic supports enhanced the metal dispersion, CeO$_2$ led to higher CO conversion below 150 °C.

The most used synthesis methods to produce noble metal supported catalysts are still wet impregnation and deposition-precipitation,[19–24] but alternative methods have been addressed, seeking for better catalysts. In particular, there is an increasing interest in synthesis methods in which the metallic phase stays encapsulated in the support, aiming to enhance the metal-support interaction and the resistance against sintering of the metallic phase. Among the methods for this purpose, stands out the synthesis of core–shell structures and the sol–gel synthesis in which the metal precursors are added during the gelation step.[25–29] As a drawback, these methods usually lead to loss of accessibility of the metal phase. A simple way to minimize this problem is to add a light agent during the synthesis, such as a carbon source, that is eliminated by calcination creating accessible paths to the encapsulated metal phase. One of the pioneering works using this approach was done by Joo et al.[27] when they synthesized Pt nanoparticles encapsulated in SiO$_2$. In their work, tetradecyltrimethylammonium bromide protected Pt nanoparticles were prepared and encapsulated in SiO$_2$; the material was calcined to remove the capping agent creating pores in the SiO$_2$ shell and providing accessibility to the metal core. Qi et al.,[25] on the other hand, used the hydrothermal method assisted by glucose to synthesize Au–CeO$_2$ catalysts; in this synthesis method, the metal and oxide precursors were mixed with glucose and subjected to hydrothermal treatment forming a material composed by carbon ($\sim$70 wt%), dispersed metal phase, and oxide support. The elimination of the carbon matrix led to the formation of spheres with a mesoporous structure containing the metal phase. The interparticle mesoporosity of the CeO$_2$ spheres allowed the reagents to access the embedded Au phase and good results in CO oxidation reaction were demonstrated. Despite the apparent crucial role played by the elimination of the carbon matrix in the textural properties of this type of catalyst, there is a lack of studies about the calcination step and its impact in the textural properties of the final catalysts. Here, we present the results where the hydrothermal synthesis assisted by glucose was used to obtain Pt-CeO$_2$ catalysts of interest for PROX-CO reaction. Special emphasis was done to evaluate the impact of the calcination conditions to the formation of the CeO$_2$ porous support and their influence in the catalytic performance of the catalyst in PROX-CO reaction.

2. EXPERIMENTAL DETAILS

2.1. Catalyst Preparation

Catalysts synthesis was adapted from the literature,[25] varying the amount of reactants and nature of the metal precursor. Two solutions were prepared:

(i) a solution containing 0.66 g of urea (Aldrich) and 0.52 g of CeCl$_3 \cdot$7H$_2$O (Aldrich) in 26 g of water,

(ii) a solution containing 2.8 g of glucose (Aldrich), 45.0 g of water and 1.35 mL of a 10 mmol $\cdot$ L^{-1} aqueous solution of K$_2$PtCl$_4$ (Aldrich); they were left stirring for 15 min separately. The first solution was slowly added to the second solution containing the platinum precursor under stirring and the final solution was left stirring for another 15 min. The Pt:Ce molar ratio was $\sim$0.01 (1 wt% Pt-CeO$_2$). The final solution was transferred to an autoclave with an internal teflon vessel of 100 mL and kept at 160 °C for 20 h. After cooling, the final solid was vacuum filtered and dried at 100 °C for 12 h; this dried sample was named C-Pt/Ce and used to evaluate the influence of calcination temperature and holding time, Table I. All samples were calcined under 100 mL $\cdot$ min^{-1} of air and heated at 1 °C $\cdot$ min^{-1} to the final temperature. The catalysts were named Pt/CeX-Y, where X is the final temperature and Y is the holding time, after achieving the final temperature.

2.2. Catalyst Characterization

Thermogravimetric analysis (TG) and X-ray diffraction (XRD) were used to monitor the carbon matrix burning and the formation of CeO$_2$ crystalline phase in all samples. The weight loss profiles of the C-Pt/Ce sample under different conditions were obtained in a TA Instruments SDT Q600 under 100 mL $\cdot$ min^{-1} of air. The sample was heated up to 1000 °C at 10 °C $\cdot$ min^{-1} to evaluated the main weight loss events. Then, additional experiments were performed to evaluate the calcination protocols, using similar conditions to the ones described in Table I. XRD patterns were obtained in Shimadzu XRD 7000 diffractometer operating at 40 kV and 30 mA and the patterns were recorded from 20 to 90° at 2.0° $\cdot$ min^{-1}.

The final platinum contents in all catalysts were experimentally confirmed by X-ray fluorescence

Table I. Calcination conditions evaluated in this work. Ramp 1 °C $\cdot$ min^{-1}.

Samples	Final temperature (°C)	Holding time (h)*
Pt/Ce250-0	250	0
Pt/Ce250-6	250	6
Pt/Ce350-0	350	0
Pt/Ce350-6	350	6
Pt/Ce450-0	450	0
Pt/Ce450-6	450	6
Pt/Ce600-0	600	0
Pt/Ce600-6	600	6

Note: *After reaching the final temperature.

spectroscopy (XRF) in a Shimadzu XRF 1800 spectrophotometer operating with a Rh source. Samples were prepared as pellets to obtain a better homogeneity of the analyzed surface.

Selected samples (Pt/Ce350-0, Pt/Ce350-6, Pt/Ce600-0 and Pt/Ce600-6) were also evaluated by N$_2$ adsorption–desorption isotherms and transmission electron microscopy (TEM) to address in more detail their textural properties. N$_2$ adsorption/desorption data were measured in a Micrometrics ASAP 2020, in which approx. 0.20 g of each sample was pre-treated at 200 °C for 2 h under N$_2$ prior the analysis. TEM images were obtained in a JEOL TEM-MSC 2100 200 KV at the Brazilian Nanoscience and Nanotechnology Laboratory–LNNano, Campinas, Brazil.

Fourier Transformed Infrared (FTIR) spectra were collected in an Agilent Cary 630 spectrophotometer using an attenuated total reflectance accessory (ATR). UV-Vis spectra by diffuse reflectance were acquired in an Agilent Cary 5000 spectrophotometer using the support (CeO$_2$) as a blank.

Temperature programmed reduction (TPR) was measured in a Micromeritics AutoChem 2920 instrument equipped with a TCD (Thermal Conductivity Detector). Before the measurements, the samples were pre-treated under N$_2$ flow at 200 °C and kept at this temperature for 1 h. They were cooled down to 50 °C, N$_2$ was replaced by 5% H$_2$ in He, and heated to 1000 °C at 10 °C·min^{-1}. H$_2$ was quantified using a calibration curve built using CuO$_2$ as a standard.

2.3. Catalytic Activity

PROX-CO reactions were performed in a vertical tubular quartz reactor loaded with 50 mg of catalyst diluted on 150 mg of quartz powder under 100 mL·min^{-1} of 1 vol.% CO, 1 vol.% O$_2$, 70 vol.% H$_2$ and He for balance. The gas effluent was analyzed by gas chromatography (Agilent 7890A GC) equipped with two capillary columns (an HP-Plot Q column, to separate CO$_2$ from the gas mixture, and an HP-Plot MoleSieve column, to separate O$_2$, N$_2$, CO and H$_2$). Before the reaction, the catalyst was reduced *in situ* under 30 mL·min^{-1} of H$_2$ at 400 °C for 1 h and cooled down to room temperature under the same atmosphere. The reaction was performed in the temperature range of 50–200 °C and CO conversion (X_{CO}), O$_2$ conversion (X_{O_2}) and CO$_2$ selectivity (S_{CO_2}) were calculated by Eqs. (1)–(3), respectively.

$$X_{CO} = \frac{CO_{in} - CO_{out}}{CO_{in}} \cdot 100 \qquad (1)$$

$$X_{O_2} = \frac{O2_{in} - O2_{out}}{O2_{in}} \cdot 100 \qquad (2)$$

$$S_{CO_2} = \frac{1}{2} \cdot \frac{X_{CO}}{X_{O_2}} \cdot 100 \qquad (3)$$

3. RESULTS AND DISCUSSION

In the hydrothermal method assisted by glucose, metal and oxide precursors are mixed with glucose forming a powder sample composed by sub-micrometric particles in which the major component is carbon (∼70%).[25] Therefore, the first step to design the Pt-CeO$_2$ catalysts was to better understand the impact of the calcination step on the textural and structural properties of the final catalyst. Figure 1 shows the overall weight loss profile obtained by TG analysis of the C-Pt/Ce sample. The first event below 100 °C was due to the elimination of water and corresponded to ∼10% of the weight loss. On the other hand, the main weight loss, associated to the carbon matrix, took place between 200–400 °C, corresponding to 70–80% of the initial weight.

The formation of carbon spheres from glucose involves the glucose polymerization during the hydrothermal treatment where the core is formed by condensation of aromatics groups and the surface contains hydroxyl groups (–OH) and carbonyl groups (–C=O).[30] Hence, the first two main events of weight loss observed between 200 and 350 °C, better identified through the derivate curve in Figure 1, could be assigned to the loss of surface groups and degradation of polysaccharides. They were followed by the third main event between 350 and 400 °C, assigned to the core burning. It is worth pointing out that the observed temperature of the core elimination was lower than the values typically found in the synthesis of hollow oxide structures (CeO$_2$, TiO$_2$, CoO, NiO) synthesized by a similar method.[31] While in the synthesis of hollow structures the carbon spheres are used as template and are covered by the metal oxide layer, in the C-Pt/Ce sample the oxide nuclei were dispersed in the carbon matrix, which favored the oxidation and burning of the carbonaceous material at lower temperatures.

Based on this TG result, the C-Pt/Ce sample was subjected to different calcination conditions, described in Table I. In detail, TG data (Table II) showed that at low temperatures, 250 °C, the weight loss progressed slowly with time indicating an incomplete burning even after holding at the final temperature for 6 h. In contrast,
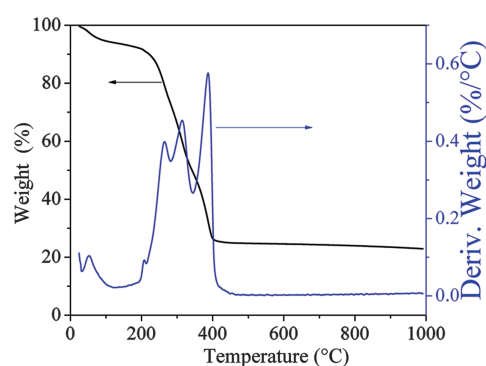

Figure 1. TG analysis showing the weight loss profile of the C-Pt/Ce sample up to 1000 °C (10 °C min^{-1}).

Table II. Weight loss and crystallite size domains (obtained by the Scherrer equation) at different calcination conditions.

| Samples	Weight loss (%)	Crystallite size (nm)
Pt/Ce250-0	58	5.7
Pt/Ce250-6	66	6.2
Pt/Ce350-0	71	6.3
Pt/Ce350-6	71	6.6
Pt/Ce450-0	71	6.9
Pt/Ce450-6	71	7.7
Pt/Ce600-0	72	10.7
Pt/Ce600-6	72	12.1

at 350 °C and higher temperatures, a complete elimination of the carbonaceous matrix occurred. This was confirmed by IR spectroscopy (Fig. 2); the IR spectrum of C-Pt/Ce showed a broad band between 2000 cm^{-1} and 1000 cm^{-1} assigned to overlapping C–O bond vibrations as found typically for carbon materials derived from glucose.[30] Its intensity was significantly reduced for samples calcined above 350 °C region, in accordance with TG analysis. The weak remaining signal could be attributed to the formation of carbonate species on the CeO$_2$ surface (bands at 1520 and 1320 cm^{-1}) due to the adsorption of CO$_2$ from atmospheric air.

Elemental analysis confirmed that Pt loading in the C–Pt/Ce sample was 0.9 wt%, close to the nominal value. In this sample, no XRD peaks could be identified and the predominant scattering arose from the amorphous carbon matrix (inset Fig. 3(a)); on the other hand, all the calcined samples showed diffraction profiles matching the CeO$_2$ fluorite structure (JCPDS No. 34-0394). No peak related to platinum crystalline phases (either PtO$_2$ or Pt) could be detected indicating that the platinum stayed well dispersed in all samples. This result contrasted with the case of Au@CeO$_2$ catalysts[25] where the formation of Au nanoparticles were identified and will be discussed later.

By increasing the temperature and holding time all peaks became narrower, indicating changes in crystallite size as estimated by the Scherrer equation (Table II). It can be observed that the sample calcined at the lowest temperature/holding time (Pt/Ce250-0) showed the smallest
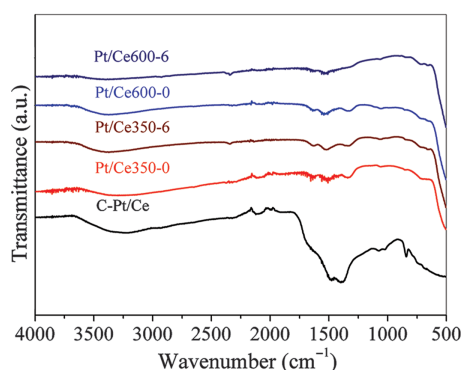
Figure 2. FTIR spectra of fresh sample (C-Pt/Ce) and calcined samples (Pt/Ce350-0, Pt/Ce350-6, Pt/Ce600-0 and Pt/Ce600-6).
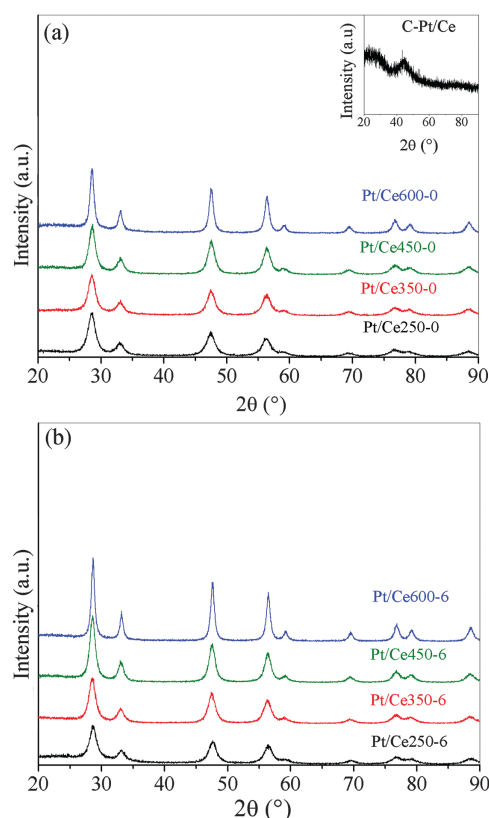
Figure 3. XRD patterns of Pt/Ce samples: (a) $t = 0$ h (at the beginning of the isotherm) and (b) $t = 6$ h (holding time at the final temperature). Inset in (a): C-Pt/Ce sample.

crystallite size (5.7 nm). In contrast, the sample calcined at the highest temperature/holding time (Pt/Ce600-6) showed the largest domain size (12.1 nm). TEM images obtained for the Pt/Ce600-6 sample showed that the material was formed by spherical aggregates of small crystallites (<20 nm); these aggregates had diameters of the order of ~200 nm (Fig. 4). This morphology was in agreement with the crystalline size derived by XRD and was similar to those obtained for Au@CeO$_2$ catalysts.[25] It is important to note that the presence of glucose is essential to the formation of these large spherical aggregates of CeO$_2$. Mai et al.[32] synthesized CeO$_2$ nanoparticles with different
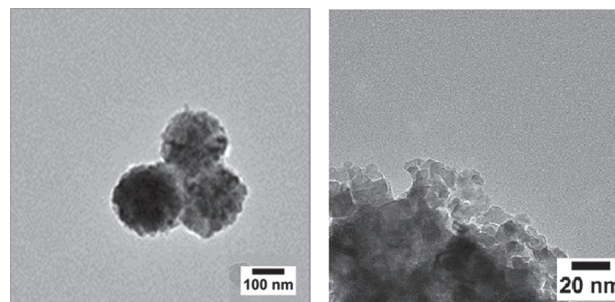
Figure 4. TEM images of Pt/Ce600-6. Note that the formation of large spherical aggregates of small CeO$_2$ crystallites.

shapes by hydrothermal synthesis at similar temperatures but in high alkaline medium and absence of glucose; while the materials exhibited similar crystalline domain sizes (10–15 nm), the final particles have anisotropic morphology, like rods and cubes, and were more compacted.

Figure 5 shows the N_2 adsorption/desorption isotherms; the samples calcined at 250 °C were not further analyzed due to the incomplete burn of the carbon matrix. All samples analyzed exhibited type II isotherms, typical of non-porous materials, with sharp increase in adsorbed volume at high relative pressures in accordance with the presence of interparticle mesopores. These mesopores were disorganized and corresponded to the spacing between the ceria crystallites that formed the large spherical aggregates observed in TEM images. As a consequence, they were related to the size and shape of the ceria crystallites and the mechanism of aggregation.[33] Table III shows the textural parameters. As expected, the specific surface area decreased with temperature and holding time due to the growth of CeO_2 crystallites, as seen by XRD. The largest value obtained for the Pt/Ce350-0 sample might indicate the presence of residual carbon (due to its higher surface area, even a small percentage of residual carbon can impact in the surface area). The pore volume and average pore diameter were similar for all samples.

UV-Vis spectroscopy was used to get information about the platinum phase in these materials. Figure 6 shows the corresponding UV-Vis spectra. These spectra were

Table III. Textural properties: Specific surface area (S_{BET}), mesopore volume (V_p) and average pore diameter (D_p).

Samples	S_{BET} (m²·g⁻¹)	V_p (BJH) (cm³·g⁻¹)	D_p (Å)
Pt/Ce350-0	106	0.13	6
Pt/Ce350-6	60	0.11	8
Pt/Ce600-0	72	0.11	8
Pt/Ce600-6	63	0.11	8

acquired using CeO_2 as blank, thereby only the platinum contribution was observed.[34] All spectra were similar and showed one broad band around 450 nm assigned to d–d transition in PtO_2.[34] Based on these results and the literature[35–37] some conclusions about the evolution of platinum oxidation state during the production of the catalyst could be drawn. At the beginning of the hydrothermal synthesis, platinum has an oxidation state of $+2$, in the form of $PtCl_4^{-2}$. The glucose is a reducing agent when in alkaline medium (in our case promoted by urea) (Eq. (4)) and has been widely used in the synthesis of gold,[38, 39] silver,[40] and copper[41] nanoparticles, for example. However, it is not strong enough to reduce platinum atoms at room temperature[37] but can be used to produce Pt nanoparticles at 100 °C.[35, 36] Considering that the hydrothermal treatment was performed at 160 °C, Pt nanoparticles were likely formed at this stage. During the calcination, the material was exposed to oxidizing atmosphere at high temperatures, and it has been shown in the literature that platinum
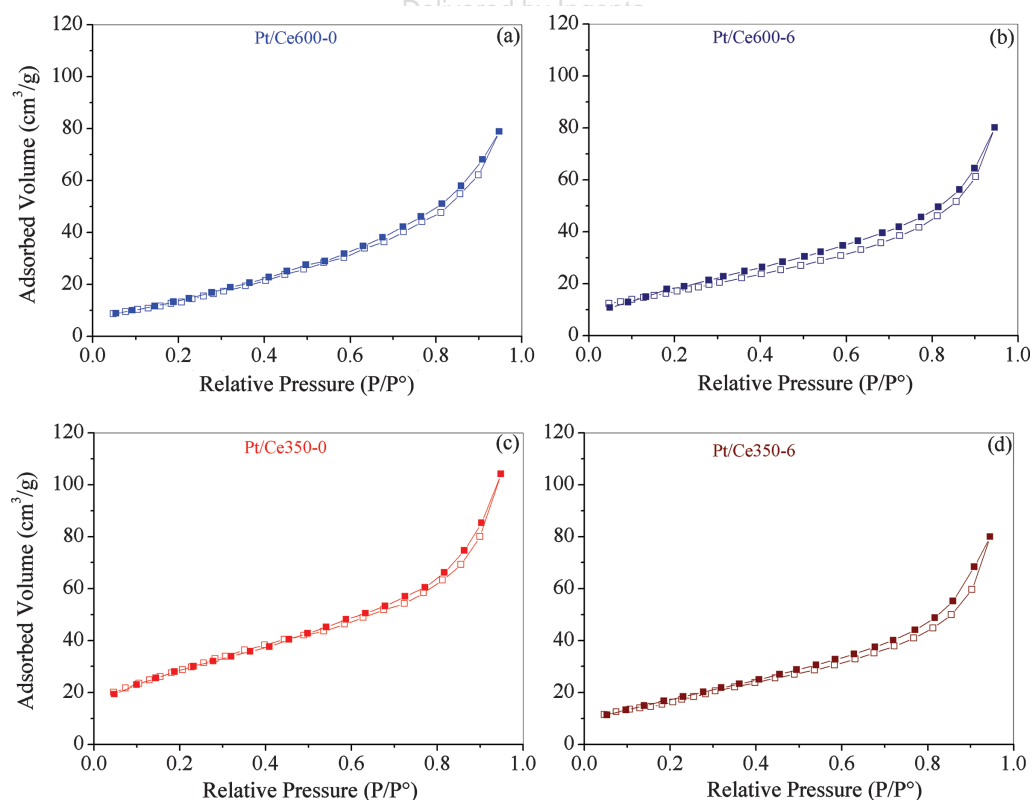
Figure 5. Adsorption (full symbols)/desorption (open symbols) N_2 isotherms: (a) Pt/Ce600-0, (b) Pt/Ce600-6, (c) Pt/Ce350-0 and (d) Pt/Ce350-6.
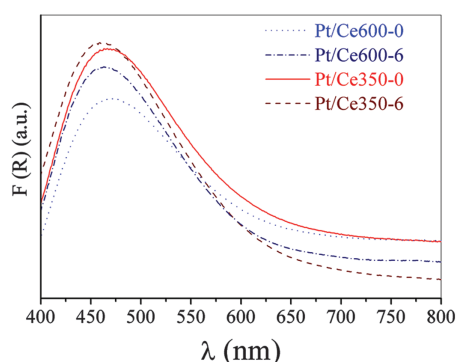
Figure 6. UV-Vis spectra obtained by diffuse reflectance.

nanoparticles (2–6 nm) supported on cerium oxide undergo oxidation to PtO_2 when heated treated above 450 °C.[42] This is in agreement with the UV-VIS results which showed the band features of Pt^{+4}. Finally, just before the reaction, the catalyst was activated under H_2 and changes in the oxidation state of Pt and Ce are expected; this was studied by TPR and is further discussed below.
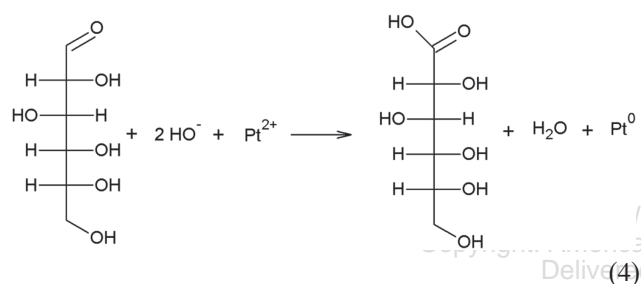

$$ (4) $$

Figure 7 shows the H_2 consumption of the catalysts during the TPR. All samples showed similar profiles that could be roughly divided in two regions. In the first region, from 100 to 600 °C, the main hydrogen consumption was assigned to reduction of Pt ions and superficial CeO_x species. Considering full reduction from Pt^{4+} to
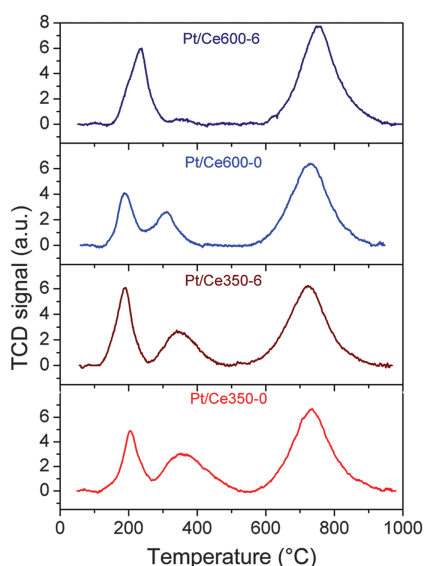

Figure 7. TPR profiles of the catalysts.

Table IV. H_2 consumption calculated from TPR, considering two different temperature ranges and the ratio between them.

	H^2 consumption (mmol $H^2 \cdot g_{cat}^{-1}$)		
Catalysts	1st region (100–600 °C)	2nd region (600–1000 °C)	Ratio (1st/2nd)
Pt/Ce350-0	0.58	0.72	0.80
Pt/Ce350-6	0.53	0.69	0.77
Pt/Ce600-0	0.39	0.70	0.56
Pt/Ce600-6	0.37	0.78	0.44

Pt^0, the maximum hydrogen consumption would be about 0.10 mmol $H_2 \cdot g_{cat}^{-1}$, which is smaller than the experimental values showed in Table IV. These results confirmed that, within this temperature range, the surface reduction of CeO_x species also occurred. In the second region, above 600 °C, the consumption was assigned to the bulk reduction of cerium. It is well established in the literature that the reduction of surface species on bare CeO_2 occurs from 400 to 600 °C; however, in the presence of metals, this reduction is typically observed at lower temperatures due to the metal-support interaction and hydrogen spilled-over from the metal to the support.[43]

Among the samples, Pt/Ce300-0, Pt/Ce350-6 and Pt/Ce600-0 showed similar TPR profiles, with two distinct events in the low temperature range and similar consumptions above 600 °C (Table IV). The Pt/Ce600-6 catalyst, on the other hand, showed a broad event below 600 °C (that might be an overlap of the two events detected in the other samples) and a hydrogen consumption slightly higher above 600 °C. The occurrence of two events at low temperature may indicate the presence of two different CeO_x species: CeO_x species directly bonded to Pt atoms, reducing at lower temperatures[19] (in the 100–300 °C range), and superficial CeO_x species, reducing at mild conditions (in the 300–600 °C range). We cannot rule out, however, the existence of an amorphous-like phase of CeO_x, not detected by XRD, which could also be reduced in this temperature range. The smaller H_2 consumption in the 1st region (Table IV) for the Pt/Ce600-0 and Pt/Ce600-6 may be related to the more ordered CeO_x phase, induced by the high temperature of calcination. Indeed, the ratio between the hydrogen consumptions in the two temperature ranges (Table IV) gave interesting insights about the catalysts in which samples calcined at lower temperature or shorter times present higher values. The ratio between the two regions of reduction correlated with the amount of Ce atoms on the surface and in the bulk and, consequently, with particle size. For Pt/Ce350-0 and Pt/Ce350-6 the ratios were similar (0.80 and 0.77) which was coherent with their crystalline domain sizes (6.3 and 6.6 nm). The ratios for Pt/Ce350-0 and Pt/Ce350-6 were larger than the ratios observed for Pt/Ce600-0 and Pt/Ce600-6 (0.56 and 0.44), which correlated well with their bigger crystalline domains (10.9 and 12.1 nm). This was a direct
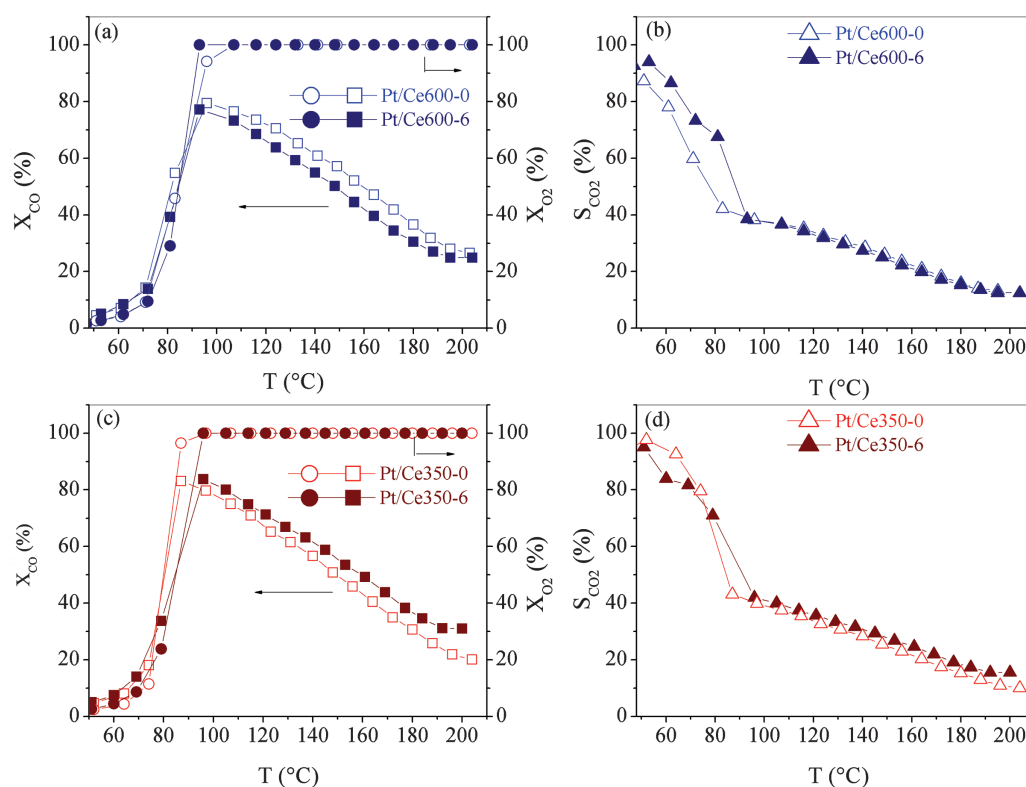
Figure 8.   (a, c) CO conversion (X_{CO}) (squares) and O$_2$ conversion (X_{O_2}) (circles) for the selected catalysts under PROX-CO conditions and (b, d) corresponding CO$_2$ selectivity (S_{CO_2}).

consequence of the calcination conditions on the crystallite size and reducibility of CeO$_2$.

Finally, these samples were evaluated for PROX-CO reaction (Fig. 8). Despite the differences related to the structural and the textural properties of CeO$_2$, all tested samples presented similar catalytic performances, with maximum of CO conversion between 75 and 80% at temperatures in the range of 90 to 100 °C. These results suggest that the differences found in specific surface area, the CeO$_2$ crystalline domains, and the overall reduction profiles did not determine the catalytic activity; this would be in accordance with the most accepted mechanism proposed for PROX-CO catalyzed by Pt/CeO$_2$, where the reaction occurs mainly at the metal-support interface.[34, 44, 45] The O$_2$ conversion and selectivity to CO$_2$ for all samples showed similar profiles: When the CO conversion reached its maximum it was accompanied by a decrease in CO$_2$ selectivity. This could be associated to the dominant CO coverage at low temperature that decreased at higher temperatures, favoring H$_2$ adsorption/activation and, consequently, lowering the CO$_2$ selectivity.[22] The lack of dependence with CeO$_2$ surface area was also in agreement with the work by Marino et al.;[18] they studied Cu–CeO$_2$ catalysts prepared by wet impregnation with different specific surface areas and established that this parameter did not affect the catalytic performance in PROX-CO. Considering 1 wt% Pt loading and the limit of 100% metal dispersion, the platinum atoms would occupy less than 10% of the CeO$_2$

surface area (considering 60 m$^2 \cdot$ g^{-1}). Therefore, it seems that the creation of the Pt-CeO$_x$ interfacial sites was the main factor affecting the catalytic activity, as found, for example, in other Pt-CeO$_x$ catalysts.[45] In our samples, the initial interaction of the Pt and Ce precursors in the reaction medium containing glucose was likely to rule the creation of these interfacial sites, and the calcination conditions, although affecting the ceria structural and textural properties, did not have a significant impact in the catalytic activity.

4. CONCLUSION

In this work we explored the hydrothermal synthesis assisted by glucose to produce Pt-CeO$_2$ catalysts of interest in PROX-CO reaction. The calcination procedure for these materials is of utmost importance for the formation of the mesoporous structure of CeO$_2$. We found that both temperature and holding time at isotherm conditions favored the increase of the CeO$_2$ crystalline domains, from ∼6 nm at 250 °C and no holding time to ∼12 nm at 600 °C and holding time of 6 h. These parameters also affected the surface area that decreased for calcinations at higher temperature or holding time. At 250 °C, the carbon matrix was not totally eliminated and the results showed that calcination at 350 °C and no holding time optimized the time and led to an active catalyst with the smallest CeO$_2$ crystalline domains. Interesting, the catalytic performance in PROX-CO were similar to

catalysts obtained at higher temperatures and holding time indicating that the available catalytic sites were not deeply affected by the modifications of the ceria matrix induced by the different calcination conditions. These results pointed out that the catalytic performance was mostly determined by metal-support interfacial sites, likely originated during the synthesis conditions, and that a mild calcination was sufficient to remove the carbon matrix and to produce an active catalyst.

References and Notes

1. R. Kydd, D. Ferri, P. Hug, J. Scott, W. Y. Teoh, and R. Amal, *J. Catal.* 277, 64 (**2011**).
2. J.-Y. Jang, C.-H. Cheng, and Y.-X. Huang, *Int. J. Hydrogen Energy* 37, 13797 (**2012**).
3. A. Hassan, V. A. Paganin, and E. A. Ticianelli, *Appl. Catal. B Environ.* 165, 611 (**2015**).
4. H. Zhang, D. Lin, G. Xu, J. Zheng, N. Zhang, Y. Li, and B. H. Chen, *Int. J. Hydrogen Energy* 40, 1742 (**2015**).
5. M. Miyamoto, M. Arakawa, Y. Oumi, and S. Uemiya, *Int. J. Hydrogen Energy* 40, 2657 (**2015**).
6. A. L. A. Marinho, R. C. Rabelo-Neto, F. B. Noronha, and L. V. Mattos, *Appl. Catal. A Gen.* 520, 53 (**2016**).
7. G. Guan, M. Kaewpanha, X. Hao, and A. Abudula, *Renew. Sustain. Energy Rev.* 58, 450 (**2016**).
8. J. D. S. L. Fonseca, H. S. Ferreira, N. Bion, L. Pirault-Roy, M. D. C. Rangel, D. Duprez, and F. Epron, *Catal. Today* 180, 34 (**2012**).
9. L. Ilieva, P. Petrova, G. Pantaleo, R. Zanella, L. F. Liotta, V. Georgiev, S. Boghosian, Z. Kaszkur, J. W. Sobczak, W. Lisowski, A. M. Venezia, and T. Tabakova, *Appl. Catal. B Environ.* 188, 154 (**2016**).
10. L. F. Córdoba and A. Martínez-Hernández, *Int. J. Hydrogen Energy* 40, 16192 (**2015**).
11. J. Xu, X.-C. Xu, L. Ouyang, X.-J. Yang, W. Mao, J. Su, and Y.-F. Han, *J. Catal.* 287, 114 (**2012**).
12. O. Pozdnyakova, D. Teschner, A. Wootsch, J. Krohnert, B. Steinhauer, H. Sauer, L. Toth, F. Jentoft, A. Knopgericke, and Z. Paal, *J. Catal.* 237, 1 (**2006**).
13. S. Rico-Francés, E. O. Jardim, T. A. Wezendonk, F. Kapteijn, J. Gascon, A. Sepúlveda-Escribano, and E. V. Ramos-Fernandez, *Appl. Catal. B Environ.* 180, 169 (**2016**).
14. Y. Chou and Y. Chen, *J. Nanosci. Nanotechnol.* 16, 9104 (**2016**).
15. T.-S. Nguyen, F. Morfin, M. Aouine, F. Bosselet, J.-L. Rousset, and L. Piccolo, *Catal. Today* 253, 106 (**2015**).
16. F. Mariño, C. Descorme, and D. Duprez, *Appl. Catal. B Environ.* 54, 59 (**2004**).
17. C.-Y. Huang, Y.-Y. Chen, C.-C. Su, and C.-F. Hsu, *J. Power Sources* 174, 294 (**2007**).
18. F. Mariño, C. Descorme, and D. Duprez, *Appl. Catal. B Environ.* 58, 175 (**2005**).
19. Q.-Y. Chen, N. Li, M.-F. Luo, and J.-Q. Lu, *Appl. Catal. B Environ.* 127, 159 (**2012**).
20. E. O. Jardim, S. Rico-Francés, F. Coloma, J. A. Anderson, J. Silvestre-Albero, and A. Sepúlveda-Escribano, *J. Colloid Interface Sci.* 443, 45 (**2015**).
21. E. O. Jardim, S. Rico-Francés, F. Coloma, J. A. Anderson, E. V. Ramos-Fernandez, J. Silvestre-Albero, and A. Sepúlveda-Escribano, *Appl. Catal. A Gen.* 492, 201 (**2015**).
22. C. S. Polster, R. Zhang, M. T. Cyb, J. T. Miller, and C. D. Baertsch, *J. Catal.* 273, 50 (**2010**).
23. K. Y. Koo, U. H. Jung, and W. L. Yoon, *Int. J. Hydrogen Energy* 39, 5696 (**2014**).
24. F. Pilger, A. Testino, M. A. Lucchini, A. Kambolis, M. Tarik, M. El Kazzi, Y. Arroyo, M. D. Rossell, and C. Ludwig, *J. Nanosci. Nanotechnol.* 25, 3530 (**2015**).
25. J. Qi, J. Chen, G. Li, S. Li, Y. Gao, and Z. Tang, *Energy Environ. Sci.* 5, 8937 (**2012**).
26. D. D. Lekeufack, A. Brioude, A. Mouti, J. G. Alauzun, P. Stadelmann, A. W. Coleman, and P. Miele, *Chem. Commun. (Camb).* 46, 4544 (**2010**).
27. S. H. Joo, J. Y. Park, C.-K. Tsung, Y. Yamada, P. Yang, and G. A Somorjai, *Nat. Mater.* 8, 126 (**2009**).
28. C. M. Y. Yeung, F. Meunier, R. Burch, D. Thompsett, and S. C. Tsang, *J. Phys. Chem. B* 110, 8540 (**2006**).
29. C. M. Y. Yeung and S. C. Tsang, *J. Mol. Catal. A Chem.* 322, 17 (**2010**).
30. M. Li, W. Li, and S. Liu, *Carbohydr. Res.* 346, 999 (**2011**).
31. X. Sun, J. Liu, and Y. Li, *Chem. Eur. J.* 12, 2039 (**2006**).
32. H. Mai, L. Sun, Y.-W. Zhang, R. Si, W. Feng, H. Zhang, H.-C. Liu, and C.-H. Yan, *J. Phys. Chem. B* 109, 24380 (**2005**).
33. K. Sing, *Colloids Surfaces A Physicochem. Eng. Asp.* 188, 3 (**2001**).
34. K. C. Petallidou and A. M. Efstathiou, *Appl. Catal. B Environ.* 140–141, 333 (**2013**).
35. Y. Shin, I.-T. Bae, and G. J. Exarhos, *Colloids Surfaces A Physicochem. Eng. Asp.* 348, 191 (**2009**).
36. C. Engelbrekt, K. H. Sørensen, T. Lübcke, J. Zhang, Q. Li, C. Pan, N. J. Bjerrum, and J. Ulstrup, *J. Chem. Phys. Phys. Chem.* 11, 2844 (**2010**).
37. J. Liu, P. Raveendran, G. Qin, and Y. Ikushima, *Chem. Commun.* 23, 2972 (**2005**).
38. K. Pacławski, B. Streszewski, W. Jaworski, M. Luty-Błocho, and K. Fitzner, *Colloids Surfaces A Physicochem. Eng. Asp.* 413, 208 (**2012**).
39. J. Liu, G. Qin, P. Raveendran, Y. Ikushima, and Y. Ikushima, *Chemistry* 12, 2131 (**2006**).
40. P. Vasileva, B. Donkova, I. Karadjova, and C. Dushkin, *Colloids Surfaces A Physicochem. Eng. Asp.* 382, 203 (**2011**).
41. M. Jin, G. He, H. Zhang, J. Zeng, Z. Xie, and Y. Xia, *Angew. Chem. Int. Ed. Engl.* 50, 10560 (**2011**).
42. J. A. van Bokhoven, C. Paun, and J. Singh, *J. Phys. Chem. C* 118, 13432 (**2014**).
43. L. Torrente-Murciano and F. R. Garcia-Garcia, *Catal. Commun.* 71, 1 (**2015**).
44. O. Pozdnyakova-Tellinger, D. Teschner, J. Krohnert, F. C. Jentoft, A. Knop-Gericke, R. Schlogl, and A. Wootsch, *J. Phys. Chem. C* 111, 5426 (**2007**).
45. D. M. Meira, R. U. Ribeiro, O. Mathon, S. Pascarelli, J. M. C. Bueno, and D. Zanchet, *Appl. Catal. B Environ.* 197, 73 (**2016**).